Environmental Science & Technology

pubs.acs.org/est

Article

Partial Oxidation of FeS Nanoparticles Enhances Cr(VI) Sequestration

Yaqi Liu, Haibo Gan, Li Tian, Zhenhai Liu, Yunyun Ji, Tong Zhang,* Pedro J. J. Alvarez, and Wei Chen

Cite This: *Environ. Sci. Technol.* 2022, 56, 13954−13963

Read Online

ACCESS | Metrics & More | Article Recommendations | Supporting Information

ABSTRACT: Iron sulfide nanoparticles (nano-FeS) have shown great potential for in situ remediation of Cr(VI) pollution by reducing Cr(VI) to the less soluble and toxic Cr(III). However, material oxidation that inevitably occurs during storage and application alters its reactivity. Herein, we show that partial oxidation of nanoparticulate mackinawite (FeS) significantly enhances its capability in sequestering Cr(VI). Oxidation of nano-FeS increases its binding affinity to Cr(VI), likely due to preferential inner-sphere complexation of Cr(VI) oxyanions to ferric over ferrous iron in mackinawite/lepidocrocite (FeS/γ-FeOOH) nanocomposites. A trade-off is that oxidation mitigates Cr(VI) reduction by lowering the electron-donating potential of the material and the electron transfer at a solution−material interface and consequently hinders the transformation of adsorbed Cr(VI) to Cr(III). Notably, the rate-limiting step of Cr(VI) sequestration transitions from adsorption to reduction during oxidation, as demonstrated with batch experiments coupled with kinetic modeling. Thus, an optimum oxidation degree exists, wherein the gain in the overall performance from enhanced adsorption overcompensates the loss from inhibited reduction, resulting in maximum sequestration of aqueous Cr(VI) as solid-phase Cr(III). Our findings inform better assessment and design of nanomaterials for Cr(VI) remediation and may be extended to interactions of other oxyanions with natural and engineered nanoparticles during oxidative aging.

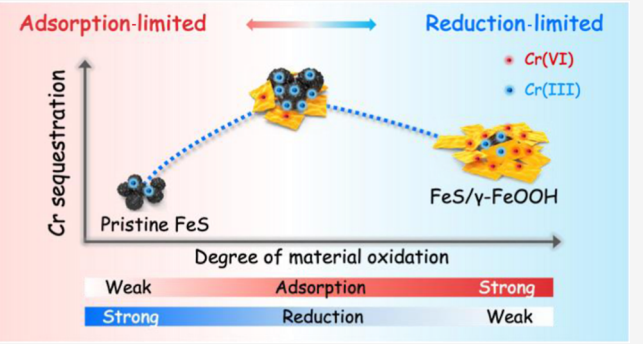

KEYWORDS: *Cr sequestration, iron sulfide nanoparticles, oxidative aging, binding affinity, electron transfer*

INTRODUCTION

Chromium (Cr) is a prevalent heavy-metal contaminant released from both natural and anthropogenic sources, such as weathering of Cr-containing minerals (e.g., chromite and crocoite) and discharge of industrial wastes.[1−3] At present, annual Cr emissions exceed international guidelines on a global scale, and the emissions from natural sources alone are over 8.9 × 10^6 kg per year.[1,4,5] As a result, Cr concentrations detected from various environmental samples, including irrigation water, secondary effluent, surface water, groundwater, soils, aquatic organisms, and crops, frequently exceed the safety threshold.[6−12] The ecological and health risks of Cr pollution heavily depend on the oxidation state of Cr.[13] Hexavalent chromium, Cr(VI), is highly soluble and toxic and has been categorized as a first-class carcinogenic substance,[14] while trivalent chromium, Cr(III), is relatively insoluble and benign.[15] Nanoparticulate iron sulfide (nano-FeS) has shown great potential for in situ remediation of Cr(VI) pollution as it is highly effective in reductively sequestering Cr(VI) from the aqueous phase to form Cr(III)-containing minerals that are not prone to reoxidation.[16−20]

Nano-FeS is susceptible to oxidative aging during storage and utilization,[21,22] resulting in altered reactivity toward target contaminants. Partial oxidation of nano-FeS was observed when stored in an anaerobic chamber[23] and en route to the site upon exposure to a trace level of oxygen.[24] During the application of nano-FeS for remediating anoxic water contaminated by trichloroethylene and heavy metals, nano-FeS gradually transformed into ferric iron-containing minerals, such as lepidocrocite.[25−28] Yet, the reported effects of nano-FeS oxidation on its contaminant removal efficiencies have been inconsistent. For example, oxidation of nano-FeS enhanced the removal of arsenic, antimony, and tungsten,[29,30] whereas it decreased the sequestration capacity for molybdenum and mercury.[29,31] Oxidative aging of Fe(0)/FeS nanocomposites slightly promoted the reductive dechlorination of trichloroethylene, but a sharp decrease in dechlorination efficiency was observed after an extended period of time.[32] To date, the mechanisms governing the interactions between

Received: April 6, 2022
Revised: August 9, 2022
Accepted: September 9, 2022
Published: September 22, 2022

oxidized nano-FeS and Cr(VI) remain unclear, which hinders rational design and accurate performance assessment of these materials for Cr(VI) remediation.

This study addresses the influence of the oxidative aging processes of nano-FeS on Cr(VI) sequestration from a mechanistic perspective under environmentally relevant conditions (pH 5.0−9.0). We first simulated environmental oxidation of nano-FeS and obtained FeS/γ-FeOOH nanocomposites with progressing degrees of oxidation (i.e., Lep %). Pristine and partially oxidized nano-FeS were reacted with Cr(VI) under different pH conditions, and the experimental data were fitted to a kinetic model to determine the rate-limiting step. The adsorption and reduction of Cr(VI) by the partially oxidized nano-FeS were also assessed using spectroscopic and electrochemical techniques, as well as by theoretical calculations, to elucidate the mechanisms of the enhanced Cr(VI) sequestration by the nanocomposites, relative to pristine nano-FeS. Our findings inform the sustainable design of remediation materials and strategies by advancing understanding of the aging effects on nanoparticle−contaminant interactions.

MATERIALS AND METHODS

Synthesis and Characterization of Pristine and Partially Oxidized Nano-FeS. Nano-FeS was prepared and oxidized prior to material characterization (see details in the Supporting Information). The particle morphology and elemental composition of pristine and partially oxidized nano-FeS were examined using field-emission transmission electron microscopy (TEM), energy-dispersive X-ray spectroscopy, high-angle annular dark field, and elemental mapping (JEM-2800, JEOL, Japan). The crystal structure was determined by powder X-ray diffraction (XRD, Ultima IV, Rigaku, Japan) with Cu Kα radiation (λ = 1.5418 Å), high-resolution TEM (HR-TEM), and selected-area electron diffraction (SAED, JEM-2800, JEOL, Japan). Surface elemental composition was analyzed using X-ray photoelectron spectroscopy (XPS, Thermo Scientific ESCALAB 250 Xi, Thermo Fisher, USA) with monochromatic Al Kα radiation. Hydrodynamic diameter (D_h), zeta potential, and isoelectric point (pH_{pzc}) were determined on a particle size analyzer (Litesizer 500, Anton Paar, Austria). Specific surface area (SA_{BET}) was obtained from multipoint Brunauer−Emmett−Teller (BET) analysis (ASAP 2020, Micromeritics Co., USA). The mineral phases were characterized on a Wissel MS-500 Mössbauer spectrometer (Germany), using ^{57}Co/Rh as the gamma energy source in transmission geometry, equipped with a helium cryostat (Advanced Research Systems, Inc.). The powder was sealed by Kapton tape, and the Mössbauer spectra were collected at 13 K to avoid oxidation. The standard spectra were obtained using Fe foil (Amersham, England) for calibration, and the Mössbauer data were fitted with software Recoil (Ottawa, Canada) in the Voigt-based mode.

Electrochemical properties of pristine and partially oxidized nano-FeS were characterized using Tafel scan, electrochemical impedance spectroscopy (EIS), and Mott−Schottky analyses on a three-electrode system (CHI 660E, Chenhua, China) immersed in 0.2 M Na_2SO_4 solution (the initial pH of electrolyte solutions was adjusted by 0.1 M H_2SO_4 and NaOH solutions) under anaerobic conditions. The working electrode was made of 10.0 mg of pristine or partially oxidized nano-FeS in 600 μL of deoxygenated ultrapure water, 300 μL of isopropanol, and 100 μL of a 5% Nafion solution, a Pt wire counter electrode, and a Ag/AgCl reference electrode (0.1 M KCl) under acidic/natural conditions or a saturated calomel electrode under alkaline conditions. Tafel scans were conducted from −0.6 to 0 V at a scan rate of 10 mV s^{-1}[33] Mott−Schottky plots of interfacial capacitance versus potential were obtained at 200, 300, and 500 Hz.[34] EIS was performed from 10 MHz to 1000 kHz with a modulation amplitude of 5 mV.[35]

Batch Experiments for Cr(VI) Sequestration. Pristine and partially oxidized nano-FeS reacted with Cr(VI) in the dark at room temperature in an anaerobic chamber (Type A glovebox, Coy Laboratory Products Inc., USA). The reaction matrices containing 2.0 mg L^{-1} Cr(VI) and 0.1 g L^{-1} pristine or partially oxidized nano-FeS were placed in a series of 20.0 mL EPA vials. The initial pH of the reaction matrices was adjusted to 5.0−9.0 with 0.05 M NaOH and HNO_3 solutions, and Cr(VI) speciation in the reaction matrices was estimated using Visual MINTEQ (version 3.1). During the batch experiments, the EPA vials were sealed using rubber screw caps with a Teflon liner and placed on a shaker at 350 rpm for 3 h. For a subset of reaction matrices, 2.0 mg L^{-1} Cr(VI) reacted with 0.1 g L^{-1} pristine or partially oxidized nano-FeS in the presence of 5 mmol L^{-1} of 1,10-phenanthroline. Soluble Fe(II) released from pristine and partially oxidized nano-FeS was assessed under an anaerobic environment with and without Cr(VI), respectively. The concentration of soluble Fe(II) was measured on a UV−vis spectrophotometer (Spark 10 M, Tecan, Switzerland) at 510 nm, using the 1,10-phenanthroline colorimetric method.

At each time point, triplicate vials were sacrificed and centrifuged at 18,407g for 10 min. The supernatant was filtered immediately through a 0.22 μm polyethersulfone membrane, and the chemical speciation of Cr in the aqueous phase was analyzed from the filtrates using high-performance liquid chromatography (Alliance e2695, Waters, USA) coupled with inductively coupled plasma−mass spectrometry (ICP−MS) [NexION 2000, PerkinElmer, USA; high-performance liquid chromatography (HPLC)−ICP−MS]. The operating parameters for the HPLC−ICP−MS analysis are given in Table S1.

In addition, solid-phase Cr(VI) of precipitates was extracted by adding 5.0 mL of 0.15 M phosphate buffer (pH = 10.0 ± 0.1) and shaking on a rotating mixer at 350 rpm for 3 h.[36,37] The total solid-phase Cr of precipitates was obtained by digesting the materials for 24 h with 2.0 mL of aqua regia (HNO_3:HCl = 1:3, v/v). The concentrations of solid-phase Cr(VI) and total solid-phase Cr were measured using ICP−MS. The solid-phase Cr(III) was assessed using a mass balance approach. To study the crystal structure and surface composition of the pristine or partially oxidized nano-FeS after reaction with Cr(VI), subsamples of the precipitates were collected and freeze-dried prior to analysis on XRD and XPS. To obtain molecular-level information, the interfacial reactions of Cr(VI) on pristine and partially oxidized nano-FeS were simulated according to the density functional theory (DFT, see details in the Supporting Information).

Modeling Approach. The multistep kinetic model simulation was conducted using MATLAB. We used a hybrid optimization method of the particle swarm optimization (PSO) algorithm and the Fmincon function to fit and solve the kinetic data. We randomized the initial value of solutions using the PSO algorithm to simplify its setting procedures, as described below. First, the population size was set to 1000, and the inertia weight, the self-learning factor, as well as the group

https://doi.org/10.1021/acs.est.2c02406
Environ. Sci. Technol. 2022, 56, 13954−13963

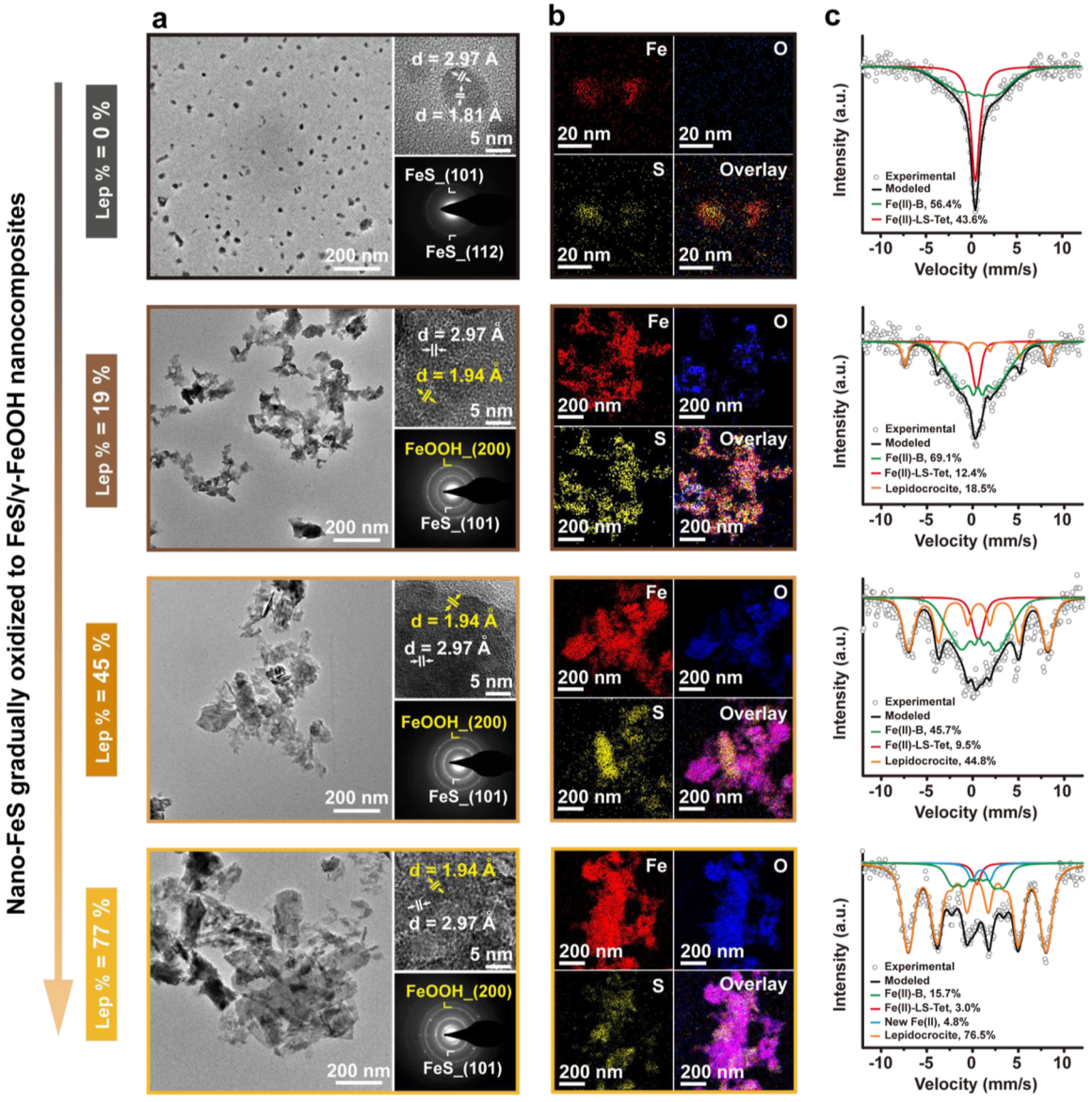

Figure 1. TEM images (a), elemental mappings (b), and Mössbauer spectra (c) of pristine and partially oxidized nano-FeS. Insets in the TEM images include HR-TEM images and SAED patterns. The experimental data points are represented by empty circles. The elemental components and model fits of the Voigt-based mode are represented by the colored and black solid lines, respectively. The relative abundance of each component is presented in the legend of (c).

learning factor, were set to 0.8, 0.5, and 0.5, respectively.[38,39] Then, the particle continually tracked the current local and global optimal positions (pbest, gbest) to update itself. Until two optimal values were found, the particle adjusted its speed and position and outputted the results. Finally, we inputted the results of the PSO algorithm into the Fmincon function for correction, and the final optimized values were obtained by integration of the differential equation system by means of function ode 45. All parameters were determined by minimizing the sum of squared errors, and the function was described as the sum of the relative square errors for all Cr species.[40,41] Minimization of the function was carried out by using a generalized reduced gradient.[42] A simplified algorithm representing the optimization flowchart is shown in Figure S1, and an error distribution diagram (Figure S2) was utilized to demonstrate the goodness of fit to the model. The fitted results of the kinetic modeling were also used to establish the mathematical relationships between the Lep % and the key parameters. These mathematical relationships were then substituted into the kinetic model to predict the abundances of aqueous Cr(VI) and solid-phase Cr(III) after a 180 min reaction to nano-FeS with continuously increasing oxidation degrees, using the interpolation method.

RESULTS AND DISCUSSION

Partial Oxidation of Nano-FeS Leads to Formation of FeS/γ-FeOOH Nanocomposites. Upon oxidation, the ellipsoidal mackinawite (FeS) nanoparticles gradually transformed into divergent sheet-like mackinawite/lepidocrocite (FeS/γ-FeOOH) nanocomposites, and a pseudo-core-shell structure appeared to form with the increasing oxidation degree of nano-FeS (Figures 1, S3a−c and Table S2). The formation of lepidocrocite (γ-FeOOH) was confirmed by the presence of the polycrystalline rings of lepidocrocite in SAED images (insets of Figure 1a), and the identified lattice fringe spacing that corresponded to the γ-FeOOH_(200) facet in the

https://doi.org/10.1021/acs.est.2c02406
Environ. Sci. Technol. 2022, 56, 13954−13963

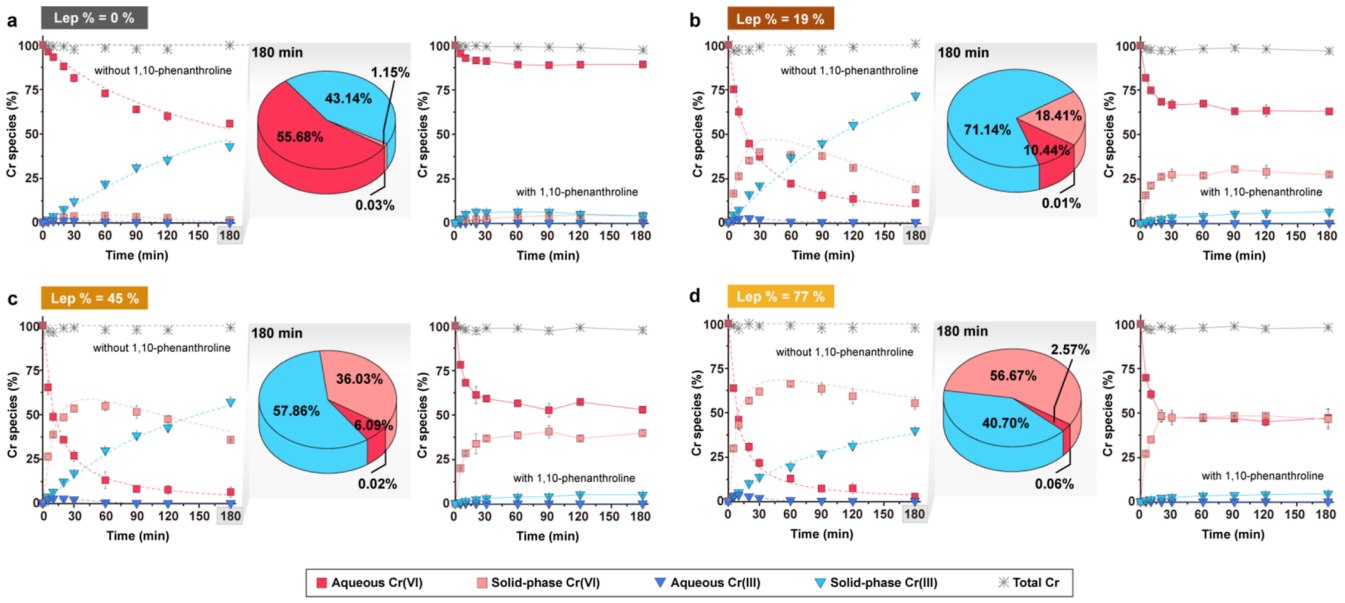

Figure 2. Abundances of different Cr species during Cr(VI) sequestration by nano-FeS with Lep % of 0 (a), 19 (b), 45 (c), and 77 % (d) in the presence/absence of 1,10-phenanthroline. The pie charts show the mass fractions of different Cr species after 180 min reactions with nano-FeS. Dotted lines represent the fitted trends according to the multistep kinetic model. Error bars represent standard deviations of triplicate samples. Reaction condition: nano-FeS concentration = 0.1 g L^{-1}, initial Cr(VI) concentration = 2.0 mg L^{-1}, 1,10-phenanthroline concentration = 5.0 mmol L^{-1}, pH = 7.0, T = 25 °C.

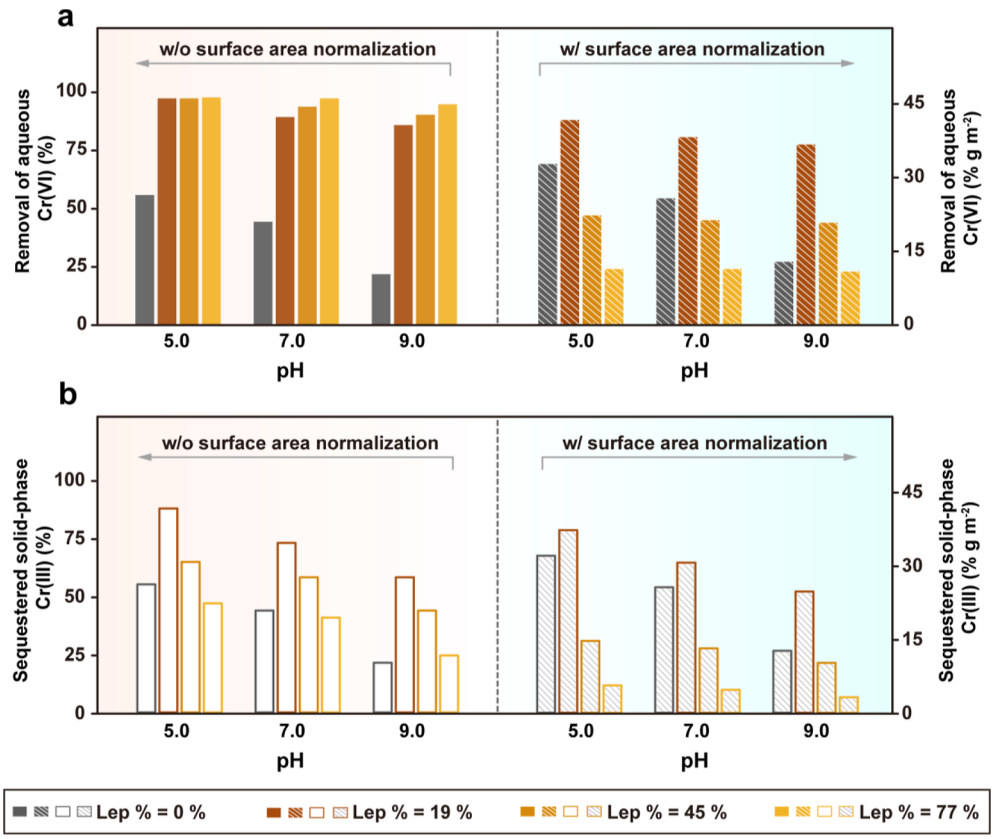

Figure 3. Removal of aqueous Cr(VI) (a) and sequestered solid-phase Cr(III) (b) after 180 min. Cr(VI) sequestration by pristine and partially oxidized nano-FeS without and with surface area normalization.

HR-TEM images (insets of Figure 1a). XRD patterns showed that γ-FeOOH was the dominant oxidation product with a pH range of 5.0−9.0, and the diffraction peaks of γ-FeOOH became more prominent with an increasing degree of oxidation (Figure S3a−c). Mössbauer spectroscopy was utilized to identify the ratio of mackinawite and lepidocrocite. The spectra of the pristine nano-FeS contained a singlet signal (labeled "Fe(II)-LS-Tet") and an additional sextet [labeled

https://doi.org/10.1021/acs.est.2c02406
Environ. Sci. Technol. 2022, 56, 13954−13963

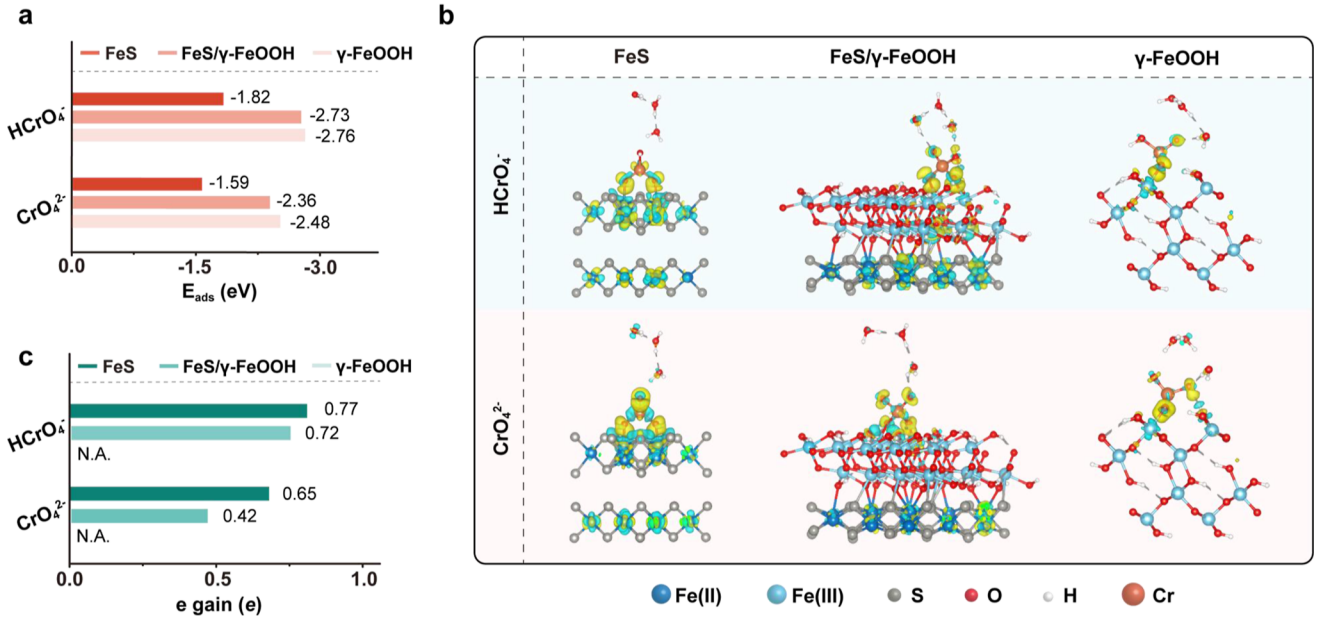

Figure 4. Adsorption energies (E_{ads}) of Cr(VI) species on FeS, FeS/γ-FeOOH, or γ-FeOOH, according to DFT calculations (a). Charge density differences of FeS, FeS/γ-FeOOH, or γ-FeOOH during $HCrO_4^-$ and CrO_4^{2-} sequestration. The yellow and cyan irregular bubbles denote electron accumulation and electron depletion, respectively (b). Bader charge analyses showing electron gain (e gain) of Cr(VI) species after adsorbing on FeS, FeS/γ-FeOOH, or γ-FeOOH (c).

"Fe(II)-B"]. As oxidation progressed, the intensity of the singlet signal gradually decreased and two additional Fe environments appeared (Figure 1c and Table S3), corresponding to new-Fe(II) and lepidocrocite, which is consistent with previous studies.[43−45] These results indicated the significant structural changes and the increase of the oxidized phase. Hereinafter, the extent of material oxidation is represented as the percentage of lepidocrocite to the total mass (Lep %), which was essentially zero for the pristine nano-FeS, and 19, 45, and 77 % for the partially oxidized materials (Figure 1c and Table S3). Further analysis of the Fe 2p and S 2p XPS spectra pointed to the transformation of Fe(II) into Fe(III) and S(II) into S_{oxi} (e.g., S_8, sulfite, or sulfate, Figure S4).

Upon material oxidation, FeS/γ-FeOOH nanocomposites were generally larger in geometric size, relative to the pristine nano-FeS (Figure 1a). Aggregation of these materials was enhanced by oxidation (Table S2), which might be partly attributed to the weaker electrostatic repulsion among monomers, as the surface sulfhydryl groups (−SH) on FeS are more prone to dissociation than the surface hydroxyl groups (−OH) on FeOOH, and subsequently, nano-FeS became less negatively charged during partial oxidation (Figure S5).[46−48] At neutral pH, the zeta potential of the pristine nano-FeS was −21.16 ± 0.61 mV, apparently lower than the zeta potential of the partially oxidized nanocomposites (−13.95 ± 0.45 ∼ −19.51 ± 0.33 mV). As the extent of oxidation increased, the specific surface area (SA_{BET}) of nano-FeS increased from 1.69 to 8.59 $m^2\ g^{-1}$ (Table S2), possibly because oxidation of nano-FeS occurred simultaneously through aqueous-phase and surface-mediated pathways that led to the formation of lepidocrocite nanosheets aggregated on the surface of the mackinawite core.[49,50]

Partial Oxidation of Nano-FeS Enhances Cr(VI) Sequestration. The partially oxidized nano-FeS was more effective than the pristine nano-FeS in Cr(VI) sequestration, as indicated by the removal of Cr(VI) from the aqueous phase and the formation of chromite ($FeCr_2O_4$) and guyanaite (CrOOH) (Figures 2, S3d−f, S6, and S7), two mineral phases with minimal solubility.[51,52] This trend prevailed over a pH range of 5.0−9.0, and Cr(VI) sequestration slightly decreased with increasing pH (Figures 3 and S3d−f), possibly due to stronger electrostatic repulsion between anionic Cr(VI) species and nano-FeS (Figures S5 and S9). After surface area normalization, the moderately oxidized material with Lep % of 19 % displayed the best performance, that is, maximum removal of aqueous Cr(VI) as well as highest accumulation of sequestered solid-phase Cr(III) (Figure 3). These results also substantiate that changes in surface properties, in addition to the increased surface area, led to enhanced Cr(VI) sequestration during partial oxidation of nano-FeS.

Formation of Cr(III) on all four materials nearly ceased upon the addition of 1,10-phenanthroline [a strong Fe(II) chelator] to block the interactions between Cr(VI) and Fe(II) (Figures 2, S6, and S7) within the pH range of 5.0−9.0. This corroborates the predominant role of Fe(II), rather than the reduced sulfur species, in driving the reduction of Cr(VI) to Cr(III) for both pristine and partially oxidized nano-FeS. Soluble Fe(II) remained below the detection limit (0.006 mg L^{-1}) in the presence of Cr(VI) (Figure S8), and the maximum concentration of soluble Fe(II) was measured to be 0.144 mg L^{-1} in the absence of Cr(VI) (Figure S8), which accounts for the reduction of up to 2.2 % of total Cr(VI). Therefore, Cr(VI) sequestration was dominated by the interface processes on nano-FeS rather than the soluble Fe(II) leached from the materials. Moreover, the addition of 1,10-phenanthroline diminished the removal of aqueous Cr(VI) via surface adsorption on pristine nano-FeS (Figures 2a, S6a, and S7a), indicating that Fe(II) was the main binding site on this material for Cr(VI). In contrast, the addition of the Fe(II) chelator only partially inhibited the adsorption of Cr(VI) on the FeS/γ-FeOOH nanocomposites, and the extent of inhibition decreased with increasing Lep % (Figures 2b−d,

https://doi.org/10.1021/acs.est.2c02406
Environ. Sci. Technol. 2022, 56, 13954−13963

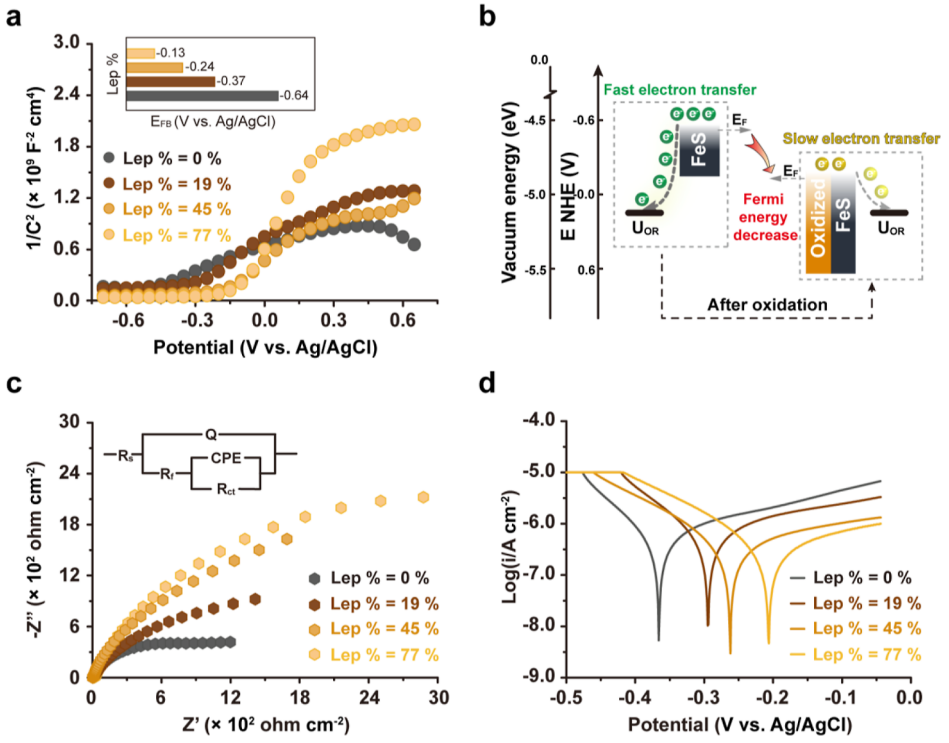

Figure 5. Mott−Schottky plots of pristine and partially oxidized nano-FeS. The inset shows the values of the flat band potential of the materials (a). Schematic plot of energy band diagram and corresponding electrode potentials for the electrolyte making contact with pristine and oxidized nano-FeS, illustrating the decreased level of Fermi energy of pristine nano-FeS after oxidation. E_F and U_{OR} represent the Fermi energy and the electrolyte potential, respectively (b). Electrochemical impedance spectra (EIS) (c) and Tafel scans (d) of pristine and partially oxidized nano-FeS. The inset in (c) represents the equivalent circuit model. All electrochemical tests were conducted at pH = 7.0.

S6b−d, and S7b−d). This infers that active binding sites for Cr(VI) continuously emerged during the oxidation of nano-FeS.

Oxidation of Nano-FeS Enhances Binding Affinity but Mitigates Electron Transfer to Cr(VI). To unravel the mechanisms controlling the dependence of the enhanced Cr(VI) sequestration on the oxidation degree of nano-FeS, we carried out theoretical calculations using three basic model structures, FeS, FeS/γ-FeOOH, and γ-FeOOH, which represent pristine, partially oxidized, and fully oxidized nano-FeS, respectively. At pH 5.0−9.0, Cr(VI) speciation is dominated by $HCrO_4^-$ and CrO_4^{2-} (Figure S9), and both Cr(VI) species were included in theoretical calculations (Figures 4 and S10−S12). To simulate the reaction interface in alkaline conditions, the basic model structures of pristine and oxidized nano-FeS are covered by OH^- (Figures S11 and S12). DFT results illustrate that the optimized adsorption configurations of $HCrO_4^-$ and CrO_4^{2-} on pristine and oxidized nano-FeS are all bidentate−binuclear (Figures S10 and S12). Adsorption of Cr(VI) to γ-FeOOH and FeS/γ-FeOOH are more favorable than to FeS, suggested by the more negative adsorption energy (Figures 4a and S11a), and this is in line with the common wisdom that oxyanions preferentially form coordination bonds with Fe(III) over Fe(II).[53,54] Additionally, the values of the adsorption energy of CrO_4^{2-} on all basic model structures are less negative than those of $HCrO_4^-$ (Figures 4a and S11a), which indicates weaker Cr(VI)−material binding at basic pH conditions and corroborates the trend of declining Cr(VI) sequestration with increasing pH in our batch experiments (Figure 3). More importantly, the DFT results demonstrate that the formation of γ-FeOOH due to partial oxidation of FeS facilitates the binding of both Cr(VI) species that dominate in the environmentally relevant pH range (Figures 4a, S9, and S11a).

According to theoretical calculations along with electrochemical analyses, pristine nano-FeS and FeS/γ-FeOOH nanocomposites exhibited evidently different electronic configurations and electron transfer properties (Figures 4, 5 and S13−S20), even though mackinawite and lepidocrocite are both n-type semiconductors.[55,56] As shown in Figures 4b and S11b, electrons are transferred from pristine and partially oxidized nano-FeS to Cr(VI), and the extent of electron accumulation around Cr(VI) is lower on FeS/γ-FeOOH than on FeS, as suggested by the relatively small valence electron gain of Cr(VI) on partially oxidized materials in Bader charge analyses (Figures 4c and S11c). As expected, there was no valence electron gain of Cr(VI) on γ-FeOOH. A Mott−Schottky plot was developed since flat band potential (E_{fb}) and surface electron density (N_d) are important parameters for determining the intrinsic reducing power of n-type semiconductors.[57,58] We found that E_{fb} moved positively with the increasing oxidation degree at all tested frequencies and pH conditions (Figures 5a and S13−S17), indicating that oxidation of nano-FeS decreased the Fermi energy level and the subsequent probabilities of electrons escaping from the conduction band (Figure 5b). The Mott−Schottky plot also showed that the surface electron density of nano-FeS decreased during material oxidation (Tables S4−S6). Furthermore, EIS and Tafel scans demonstrated the oxidation-compromised electron transfer of nano-FeS in an aqueous solution from kinetic and thermodynamic points of view, respectively. The Nyquist plots, Bode plots, and corresponding

https://doi.org/10.1021/acs.est.2c02406
Environ. Sci. Technol. 2022, 56, 13954−13963

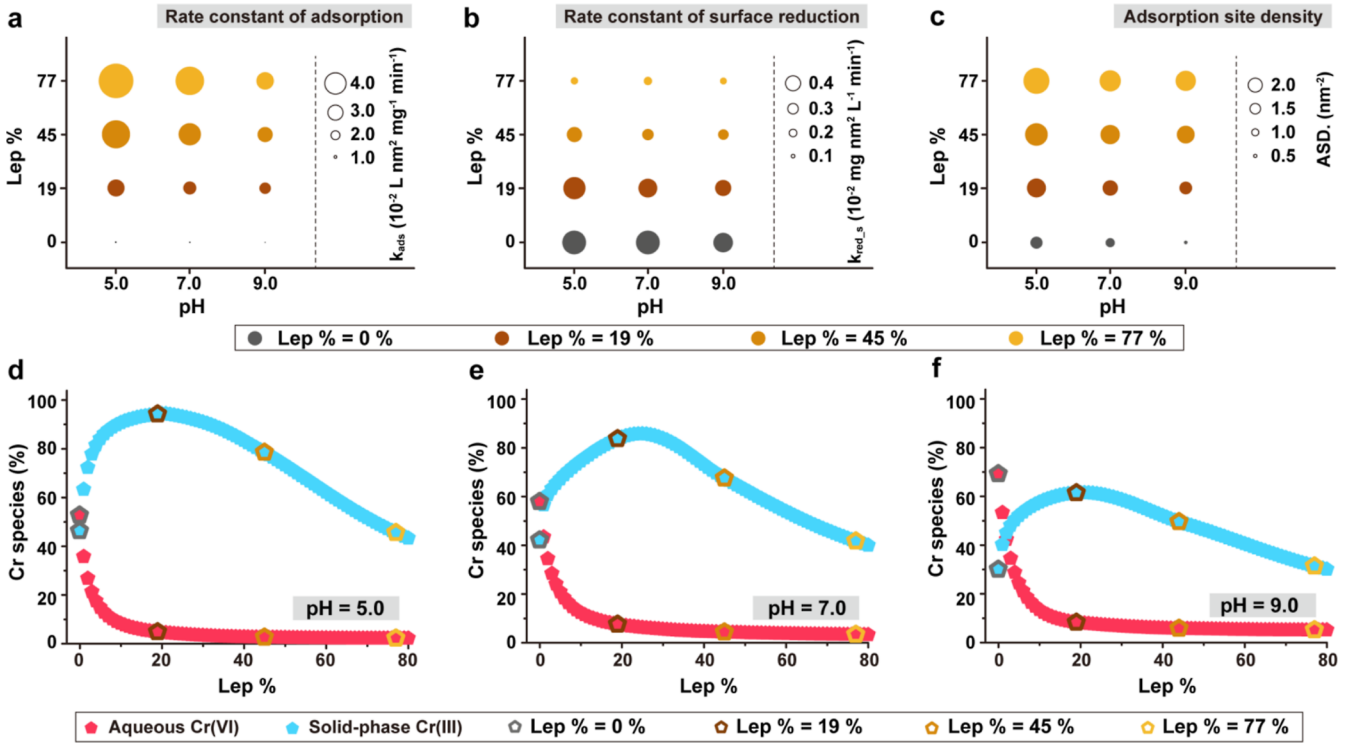

Figure 6. Fitted parameters of the multistep kinetic model at pH 5−9, including rate constant of adsorption k_{ads} (a), rate constant of surface reduction k_{red_s} (b), and adsorption site density, ASD. (c). Simulated abundances of aqueous Cr(VI) and solid-phase Cr(III) after 180 min reactions with pristine and partially oxidized nano-FeS at pH = 5.0 (d), pH = 7.0 (e), and pH = 9.0 (f). The empty symbols represent the experimental data of batch Cr(VI) sequestration by nano-FeS with Lep % of 0, 19, 45, and 77%.

equivalent circuit model revealed that charge-transfer resistance (R_{ct}), representing the resistance for electron transfer at the solution−material interface,[35,59,60] gradually increased as oxidation proceeded at pH 5.0−9.0 (Figures 5c, S13b, S14b, and S18−S20 and Tables S4−S6). The decreasing potential of electron loss from nano-FeS during material oxidation was corroborated by the measured free corrosion potentials that gradually became less negative within the range of pH 5.0−9.0 (Figures 5d, S13c, and S14c and Tables S4−S6). Therefore, oxidation of nano-FeS mitigates electron transfer processes, offsetting the benefits in Cr(VI) sequestration gained from the enhanced binding of Cr(VI). Accordingly, the overall effects of nano-FeS oxidation on Cr(VI) sequestration depend on the degree of material oxidation.

Optimal Cr(VI) Sequestration Can Be Achieved by Tuning the Oxidation Degree of Nano-FeS. An interesting observation is that Cr(VI) barely accumulated on pristine nano-FeS over the experimental period (Figures 2a, S6a, S7a, and S21−S23), whereas solid-phase Cr(VI) rapidly increased and then slowly decreased on FeS/γ-FeOOH nanocomposites at pH 5.0−9.0 (Figures 2b−d, S6b−d, and S7b−d). These results suggest that the rate-limiting step of the sequential reactions transitioned from adsorption to reduction during the oxidative aging of nano-FeS. Hence, to quantitatively assess the effects of partial oxidation on the kinetics of surface adsorption and reduction, Cr(VI) sequestration data generated with different oxidation degrees of nano-FeS were fitted to a multistep kinetic model.[40−42]

$$\frac{dC_1}{dt} = k_{ads}(C_1)^{n_1} \times (Q_1)^{m_1} - k_{red\_a}(C_1)^{n_3} \quad (1)$$

$$\frac{dC_2}{dt} = k_{red\_s}(C_2)^{n_2} \times (Q_2)^{m_2} + k_{ads}(C_1)^{n_1} \times (Q_1)^{m_1} \quad (2)$$

$$\frac{dC_3}{dt} = k_{red\_s}(C_2)^{n_2} \times (Q_2)^{m_2} + k_{prec}(C_4)^{n_4} \quad (3)$$

$$\frac{dC_4}{dt} = k_{red\_a}(C_1)^{n_3} - k_{prec}(C_4)^{n_4} \quad (4)$$

where C_1, C_2, C_3, and C_4 represent the concentrations of aqueous Cr(VI), solid-phase Cr(VI), solid-phase Cr(III), and aqueous Cr(III), respectively; k_{ads} is the adsorption rate constant of aqueous Cr(VI); k_{red_a} is the reduction rate constant of Cr(VI) in the aqueous phase; k_{red_s} is the reduction rate constant of solid-phase Cr(VI) on the surface of nano-FeS; k_{prec} is the rate of aqueous Cr(III) precipitated on the surface of nano-FeS; Q_1 and Q_2 represent the adsorption and reduction site density, respectively; n_1 and n_2 represent the reaction orders of adsorption and reduction on the surface of nano-FeS, respectively; n_3 and n_4 represent the reaction orders of reduction and precipitation in the aqueous phase, respectively; m_1 and m_2 represent the attenuation rate constants of the adsorption site and the reduction site, respectively. Indeed, the kinetics of surface adsorption and reduction, the two sequential steps that contribute to more than 90.3% of aqueous Cr(VI) removal, were both significantly influenced by the oxidation of nano-FeS (Figure 6 and Tables S7−S9). At all tested pH conditions, the adsorption rate constant (k_{ads}) markedly increased, while the surface reduction rate constant (k_{red_s}) appeared to decrease with increasing Lep % (Figure 6a,b), in line with the shifting of rate-limiting step of Cr(VI) sequestration.

https://doi.org/10.1021/acs.est.2c02406
Environ. Sci. Technol. 2022, 56, 13954−13963

Interestingly, the goodness of fit to this model (Figure S2) suggests that surface adsorption follows a second-order trend (Tables S7−S9). Thus, the adsorption site density (Q_1) that increased with oxidation (Figure 6c), together with k_{ads} (Figure 6a), points to rapid adsorption of Cr(VI) onto partially oxidized nano-FeS. In contrast, surface reduction is a zero-order reaction (Tables S7−S9), inferring that transformation to Cr(III) does not depend on the abundance of surface-bound Cr(VI). Hence, excessive accumulation of Cr(VI) on materials with large Lep % cannot enhance the production of solid-phase Cr(III), the end product of Cr(VI) sequestration, as surface reduction of Cr(VI) is merely determined by the intrinsic redox properties of nano-FeS that is susceptible to oxidation. The modeling results clearly show that under any given solution chemistry conditions (e.g., pH), there should be an optimum degree of material oxidation, at which the adsorption rate is enhanced sufficiently to prevent adsorption from being the rate-limiting step, while the inhibited electron transfer to Cr(VI) induced by oxidation is relatively small (Figure 6d−f).

Environmental Implications. Incidental or intentional oxidation of nanoparticulate reductants (e.g., nano-FeS) during manufacture, storage, and the application does not necessarily compromise their performance in environmental remediation. Our study demonstrates that partial oxidation of nano-FeS significantly enhances Cr(VI) sequestration by promoting the rate-limiting reaction of surface adsorption. The overall performance of Cr(VI) sequestration changes nonmonotonically during material oxidation, and maximum sequestration of aqueous Cr(VI) as solid-phase Cr(III) occurs at a system-specific optimum oxidation degree that varies with pH conditions. Understanding this nonmonotonical trend of Cr(VI) sequestration is critical for accurately predicting the real-world remediation processes, and identifying the "optimum" degree of material oxidation will help improve the design of functional nanomaterials for engineered applications.

The conceptual models and reaction mechanisms discovered in this study are not limited to understanding interfacial reactions between Cr and nanoparticulate mackinawite and may be extended to other problematic oxyanions containing phosphorus, arsenic, selenium, and tellurium, as well as other engineered or naturally occurring nanoparticles containing reduced iron (e.g., zero-valent iron, pyrite, magnetite, and vivianite). The mechanistic findings from our research mainly focus on postoxidation scenarios, and future research on the simultaneous reactions of Fe nanoparticles, natural oxidants, and contaminants is warranted.

■ ASSOCIATED CONTENT

Supporting Information

The Supporting Information is available free of charge at https://pubs.acs.org/doi/10.1021/acs.est.2c02406.

Additional experimental methods; error distribution histograms of model fitting; results of XRD, XPS, BET, DLS, ξ-potential, and Cr speciation analyses; adsorption configurations of Cr(VI); batch experiments of Cr(VI) sequestration at acidic and basic pH conditions as well as in the presence of 1,10-phenanthroline; and supplementary electrochemical analyses and soluble Fe(II) released from nanomaterials with and without Cr(VI) (PDF)

■ AUTHOR INFORMATION

Corresponding Author

Tong Zhang − *College of Environmental Science and Engineering, Ministry of Education Key Laboratory of Pollution Processes and Environmental Criteria, Tianjin Key Laboratory of Environmental Remediation and Pollution Control, Nankai University, Tianjin 300350, China;* orcid.org/0000-0002-8151-3697; Phone: 86-22-2350-1117; Email: zhangtong@nankai.edu.cn

Authors

Yaqi Liu − *College of Environmental Science and Engineering, Ministry of Education Key Laboratory of Pollution Processes and Environmental Criteria, Tianjin Key Laboratory of Environmental Remediation and Pollution Control, Nankai University, Tianjin 300350, China*

Haibo Gan − *College of Chemical Engineering, State Key Laboratory of Fine Chemicals, Dalian University of Technology, Dalian 116033, China*

Li Tian − *School of Resource and Environmental Engineering, Jiangxi University of Science and Technology, Ganzhou 341000, China*

Zhenhai Liu − *College of Environmental Science and Engineering, Ministry of Education Key Laboratory of Pollution Processes and Environmental Criteria, Tianjin Key Laboratory of Environmental Remediation and Pollution Control, Nankai University, Tianjin 300350, China*

Yunyun Ji − *College of Environmental Science and Engineering, Ministry of Education Key Laboratory of Pollution Processes and Environmental Criteria, Tianjin Key Laboratory of Environmental Remediation and Pollution Control, Nankai University, Tianjin 300350, China*

Pedro J. J. Alvarez − *Department of Civil and Environmental Engineering, Rice University, Houston, Texas 77005, United States;* orcid.org/0000-0002-6725-7199

Wei Chen − *College of Environmental Science and Engineering, Ministry of Education Key Laboratory of Pollution Processes and Environmental Criteria, Tianjin Key Laboratory of Environmental Remediation and Pollution Control, Nankai University, Tianjin 300350, China;* orcid.org/0000-0003-2106-4284

Complete contact information is available at: https://pubs.acs.org/10.1021/acs.est.2c02406

Notes

The authors declare no competing financial interest.

■ ACKNOWLEDGMENTS

This research was supported by the National Key Research and Development Program of China (2018YFC1800705), the National Natural Science Foundation of China (22020102004 and 22125603), the Tianjin Municipal Science and Technology Bureau (21JCJQJC00060 and 20JCZDJC00690) and the Ministry of Education of China (T2017002). Partial funding for PJJA was provided by the NSF Nanosystems Engineering Research Center for Nanotechnology-Enabled Water Treatment (ERC-1449500). We thank Qingqian Yao for assisting with XRD analysis and Shuangxi Liu and Kai Yu for assisting with electrochemical analyses.

REFERENCES

(1) Kieber, R. J.; Willey, J. D.; Zvalaren, S. D. Chromium speciation in rainwater: Temporal variability and atmospheric deposition. *Environ. Sci. Technol.* **2002**, *36*, 5321−5327.

(2) Gonzalez, A. R.; Ndung'u, K.; Flegal, A. R. Natural occurrence of hexavalent chromium in the aromas red sands aquifer, California. *Environ. Sci. Technol.* **2005**, *39*, 5505−5511.

(3) Oze, C.; Bird, D. K.; Fendorf, S. Genesis of hexavalent chromium from natural sources in soil and groundwater. *Proc. Natl. Acad. Sci. USA* **2007**, *104*, 6544−6549.

(4) Nagajyoti, P. C.; Lee, K. D.; Sreekanth, T. V. M. Heavy metals, occurrence and toxicity for plants: A review. *Environ. Chem. Lett.* **2010**, *8*, 199−216.

(5) Pacyna, J. F.; Nriagu, J. *In Chromium in the Natural and Human Environments*; Niragu, J. O., Nieboer, E., Eds.; Willey and Sons: New York, 1988; pp 105−123.

(6) Gifford, M.; Chester, M.; Hristovski, K.; Westerhoff, P. Human health tradeoffs in wellhead drinking water treatment: Comparing exposure reduction to embedded life cycle risks. *Water Res.* **2018**, *128*, 246−254.

(7) Smith, C. J.; Hopmans, P.; Cook, F. J. Accumulation of Cr, Pb, Cu, Ni, Zn and Cd in soil following irrigation with treated urban effluent in Australia. *Environ. Pollut.* **1996**, *94*, 317−323.

(8) Fuentes-Rivas, R. M.; Martin-Romero, F.; Pulido, D. G.; Oca, J. M.; Ramírez, J. A. R.; Leal, J. A. R. Chromium species and 3D-fluoresence spectroscopy in a soil irrigated with industrial wastewater. *Agric. Wastes Residues* **2018**, 29.

(9) Renner, R. Huge chromium plume threatens Colorado river. *Environ. Sci. Technol.* **2004**, *38*, 178A.

(10) McClain, C. N.; Fendorf, S.; Johnson, S. T.; Menendez, A.; Maher, K. Lithologic and redox controls on hexavalent chromium in vadose zone sediments of California's central valley. *Geochim. Cosmochim. Acta* **2019**, *265*, 478−494.

(11) Farag, A. M.; May, T.; Marty, G. D.; Easton, M.; Harper, D. D.; Little, E. E.; Cleveland, L. The effect of chronic chromium exposure on the health of Chinook salmon (Oncorhynchus tshawytscha). *Aquat. Toxicol.* **2006**, *76*, 246−57.

(12) Rai, P. K.; Lee, S. S.; Zhang, M.; Tsang, Y. F.; Kim, K.-H. Heavy metals in food crops: Health risks, fate, mechanisms, and management. *Environ. Int.* **2019**, *125*, 365−385.

(13) Zhitkovich, A. Chromium in drinking water: Sources, metabolism, and cancer risks. *Chem. Res. Toxicol.* **2011**, *24*, 1617−1629.

(14) Pavesi, T.; Moreira, J. C. Mechanisms and individuality in chromium toxicity in humans. *Appl. Toxicol.* **2020**, *40*, 1183−1197.

(15) Sivakumar, S.; Subbhuraam, C. V. Toxicity of chromium(III) and chromium(VI) to the earthworm Eisenia fetida. *Ecotoxicol. Environ. Saf.* **2005**, *62*, 93−98.

(16) Li, Y.; Wang, W.; Zhou, L.; Liu, Y.; Mirza, Z. A.; Lin, X. Remediation of hexavalent chromium spiked soil by using synthesized iron sulfide particles. *Chemosphere* **2017**, *169*, 131−138.

(17) Yu, Y. Y.; Cheng, Q. W.; Sha, C.; Chen, Y. X.; Naraginti, S.; Yong, Y. C. Size-controlled biosynthesis of FeS nanoparticles for efficient removal of aqueous Cr(VI). *Chem. Eng. J.* **2020**, *379*, 122404.

(18) Park, M.; Kim, S.; Kim, S.; Ryu, J.; Song, Y. S.; Jeong, H. Y. Cr(VI) immobilization by FeS-coated alumina and silica: Effects of pH and surface coating density. *J. Hazard. Mater.* **2022**, *421*, 126784.

(19) Patterson, R. R.; Fendorf, S.; Fendorf, M. Reduction of hexavalent chromium by amorphous iron sulfide. *Environ. Sci. Technol.* **1997**, *31*, 2039−2044.

(20) Fan, D.; Lan, Y.; Tratnyek, P. G.; Johnson, R. L.; Filip, J.; O'Carroll, D. M.; Nunez Garcia, A. N.; Agrawal, A. Sulfidation of iron-based materials: A review of processes and implications for water treatment and remediation. *Environ. Sci. Technol.* **2017**, *51*, 13070−13085.

(21) Bi, Y.; Hayes, K. F. Nano-FeS inhibits UO_2 reoxidation under varied oxic conditions. *Environ. Sci. Technol.* **2014**, *48*, 632−640.

(22) Wu, H.; Liu, Y.; Chen, B.; Yang, F.; Wang, L.; Kong, Q.; Ye, T.; Lian, J. Enhanced adsorption of molybodenum(VI) from aquatic solutions by chitosan-coated zirconium-iron sulfide composite. *Sep. Purif. Technol.* **2021**, *279*, 119736.

(23) Duan, J.; Ji, H.; Zhao, X.; Tian, S.; Liu, X.; Liu, W.; Zhao, D. Immobilization of U(VI) by stabilized iron sulfide nanoparticles: Water chemistry effects, mechanisms, and long-term stability. *Chem. Eng. J.* **2020**, *393*, 124692.

(24) Han, D. S.; Orillano, M.; Khodary, A.; Duan, Y.; Batchelor, B.; Abdel-Wahab, A. Reactive iron sulfide (FeS)-supported ultrafiltration for removal of mercury (Hg(II)) from water. *Water Res.* **2014**, *53*, 310−321.

(25) Breynaert, E.; Bruggeman, C.; Maes, A. XANES-EXAFS analysis of Se solid-phase reaction products formed upon contacting Se(IV) with FeS_2 and FeS. *Environ. Sci. Technol.* **2008**, *42*, 3595−3601.

(26) He, Y. T.; Wilson, J. T.; Wilkin, R. T. Impact of iron sulfide transformation on trichloroethylene degradation. *Geochim. Cosmochim. Acta* **2010**, *74*, 2025−2039.

(27) Dulnee, S.; Scheinost, A. C. Interfacial reaction of Sn^{II} on mackinawite (FeS). *J. Contam. Hydrol.* **2015**, *177*−*178*, 183−193.

(28) Bhattacharjee, S.; Ghoshal, S. Optimal design of sulfidated nanoscale zero-valent iron for enhanced trichloroethene degradation. *Environ. Sci. Technol.* **2018**, *52*, 11078−11086.

(29) Park, J.-H.; Kim, S.-J.; Ahn, J. S.; Lim, D.-H.; Han, Y.-S. Mobility of multiple heavy metalloids in contaminated soil under various redox conditions: Effects of iron sulfide presence and phosphate competition. *Chemosphere* **2018**, *197*, 344−352.

(30) Liu, S.; Feng, H.; Tang, L.; Dong, H.; Wang, J.; Yu, J.; Feng, C.; Liu, Y.; Luo, T.; Ni, T. Removal of Sb(III) by sulfidated nanoscale zero-valent iron: The mechanism and impact of environmental conditions. *Sci. Total Environ.* **2020**, *736*, 139629.

(31) Sun, Y.; Lou, Z.; Yu, J.; Zhou, X.; Lv, D.; Zhou, J.; Baig, S. A.; Xu, X. Immobilization of mercury (II) from aqueous solution using Al_2O_3-supported nanoscale FeS. *Chem. Eng. J.* **2017**, *323*, 483−491.

(32) Dong, H.; Zhang, C.; Deng, J.; Jiang, Z.; Zhang, L.; Cheng, Y.; Hou, K.; Tang, L.; Zeng, G. Factors influencing degradation of trichloroethylene by sulfide-modified nanoscale zero-valent iron in aqueous solution. *Water Res.* **2018**, *135*, 1−10.

(33) Hu, Y.; Peng, X.; Ai, Z.; Jia, F.; Zhang, L. Liquid nitrogen activation of zero-valent iron and its enhanced Cr(VI) removal performance. *Environ. Sci. Technol.* **2019**, *53*, 8333−8341.

(34) Liu, T.; Wang, Y.; Liu, C.; Li, X.; Cheng, K.; Wu, Y.; Fang, L.; Li, F.; Liu, C. Conduction band of hematite can mediate cytochrome reduction by Fe(II) under dark and anoxic conditions. *Environ. Sci. Technol.* **2020**, *54*, 4810−4819.

(35) Turcio-Ortega, D.; Fan, D.; Tratnyek, P. G.; Kim, E.-J.; Chang, Y.-S. Reactivity of Fe/FeS nanoparticles: Electrolyte composition effects on corrosion electrochemistry. *Environ. Sci. Technol.* **2012**, *46*, 12484−12492.

(36) Bae, S.; Sihn, Y.; Kyung, D.; Yoon, S.; Eom, T.; Kaplan, U.; Kim, H.; Schäfer, T.; Han, S.; Lee, W. Molecular identification of Cr(VI) removal mechanism on vivianite surface. *Environ. Sci. Technol.* **2018**, *52*, 10647−10656.

(37) Pan, C.; Liu, H.; Catalano, J. G.; Qian, A.; Wang, Z.; Giammar, D. E. Rates of Cr(VI) generation from $Cr_xFe_{1-x}(OH)_{(3)}$ solids upon reaction with manganese oxide. *Environ. Sci. Technol.* **2017**, *51*, 12416−12423.

(38) Sung, W.-T.; Chang, K.-Y. Health parameter monitoring via a noval wireless system. *Appl. Soft Comput.* **2014**, *22*, 667−680.

(39) Xia, X.; Gui, L.; He, G.; Wei, B.; Zhang, Y.; Yu, F.; Wu, H.; Zhan, Z.-H. An expanded particle swarm optimization based on multi-exemplar and forgetting ability. *Inform. Sci.* **2020**, *508*, 105−120.

(40) Zhang, X.; Fu, W.; Yin, Y.; Chen, Z.; Qiu, R.; Simonnot, M.-O.; Wang, X. Adsorption-reduction removal of Cr(VI) by tobacco petiole pyrolytic biochar: Batch experiment, kinetic and mechanism studies. *Bioresour. Technol.* **2018**, *268*, 149−157.

(41) Zhang, J.; Yin, H.; Chen, L.; Liu, F.; Chen, H. The role of different functional groups in a novel adsorption-complexation-reduction multi-step kinetic model for hexavalent chromium retention by undissolved humic acid. *Environ. Pollut.* **2018**, *237*, 740−746.

https://doi.org/10.1021/acs.est.2c02406
Environ. Sci. Technol. 2022, 56, 13954−13963

(42) Escudero, C.; Fiol, N.; Poch, J.; Villaescusa, I. Modeling of kinetics of Cr(VI) sorption onto grape stalk waste in a stirred batch reactor. *J. Hazard. Mater.* **2009**, *170*, 286−291.
(43) Bi, Y.; Hyun, S. P.; Kukkadapu, R.; Hayes, K. F. Oxidative dissolution of UO_2 in a simulated groundwater containing synthetic nanocrystalline mackinawite. *Geochim. Cosmochim. Acta* **2013**, *102*, 175−190.
(44) Cheng, D.; Neumann, A.; Yuan, S.; Liao, W.; Qian, A. Oxidative Degradation of Organic Contaminants by FeS in the Presence of O_2. *Environ. Sci. Technol.* **2020**, *54*, 4091−4101.
(45) Cheng, D.; Liao, W.; Yuan, S. Effect of in situ generated iron oxyhydroxide coatings on FeS oxygenation and resultant hydroxyl radical production for contaminant degradation. *Chem. Eng. J.* **2020**, *394*, 124961.
(46) Hiemstra, T.; Venema, P.; Riemsdijk, W. H. Intrinsic proton affinity of reactive surface groups of metal (Hydr)oxides: The bond valence principle. *J. Colloid Interface Sci.* **1996**, *184*, 680−692.
(47) Wolthers, M.; Charlet, L.; van Der Linde, P. R.; Rickard, D.; van Der Weijden, C. H. Surface chemistry of disordered mackinawite (FeS). *Geochim. Cosmochim. Acta* **2005**, *69*, 3469−3481.
(48) Hiemstra, T.; Van Riemsdijk, W. H. A surface structural approach to ion adsorption: The charge distribution (CD) model. *J. Colloid Interface Sci.* **1996**, *179*, 488−508.
(49) Bae, S.; Collins, R. N.; Waite, T. D.; Hanna, K. Advances in surface passivation of nanoscale zero-valent iron: A critical review. *Environ. Sci. Technol.* **2018**, *52*, 12010−12025.
(50) Jeong, H. Y.; Han, Y.-S.; Park, S. W.; Hayes, K. F. Aerobic oxidation of mackinawite (FeS) and its environmental implication for arsenic mobilization. *Geochim. Cosmochim. Acta* **2010**, *74*, 3182−3198.
(51) Liu, J.; Li, R.; Yao, Y.; Liu, A. Fate and mechanistic insights into the transformation of aged nanoscale zero-valent iron (nZVI) reacted with Cr(VI): Impact of aging time in oxic water. *ACS Earth Space Chem.* **2019**, *3*, 1288−1295.
(52) Lv, D.; Zhou, J.; Cao, Z.; Xu, J.; Liu, Y.; Li, Y.; Yang, K.; Lou, Z.; Lou, L.; Xu, X. Mechanism and influence factors of chromium(VI) removal by sulfide-modified nanoscale zero-valent iron. *Chemosphere* **2019**, *224*, 306−315.
(53) Qin, H.; Li, J.; Yang, H.; Pan, B.; Zhang, W.; Guan, X. Coupled effect of ferrous ion and oxygen on the electron selectivity of zero-valent iron for selenate sequestration. *Environ. Sci. Technol.* **2017**, *51*, 5090−5097.
(54) Jeon, B. H.; Dempsey, B. A.; Burgos, W. D.; Barnett, M. O.; Roden, E. E. Chemical reduction of U(VI) by Fe(II) at the solid-water interface using natural and synthetic Fe(III) oxide. *Environ. Sci. Technol.* **2005**, *39*, 5642−5649.
(55) Ding, J.; Zhang, L.; Lu, M.; Wang, J.; Wen, Z.; Hao, W. The electrochemical behaviour of 316L austenitic stainless steel in Cl^- containing environment under different H_2S partial pressures. *Appl. Surf. Sci.* **2014**, *289*, 33−41.
(56) Duan, Y.; Chakraborty, B.; Tiwari, C. K.; Baranov, M.; Tubul, T.; Leffler, N.; Neyman, A.; Weinstock, I. A. Solution-state catalysis of visible light-driven water oxidation by macroanion-like inorganic complexes of gamma-FeOOH nanocrystals. *ACS Catal.* **2021**, *11*, 11385−11395.
(57) Hankin, A.; Bedoya-Lora, F. E.; Alexander, J. C.; Regoutz, A.; Kelsall, G. H. Flat band potential determination: Avoiding the pitfalls. *J. Mater. Chem. A* **2019**, *7*, 26162−26176.
(58) Ahn, H.-J.; Kwak, M.-J.; Lee, J.-S.; Yoon, K.-Y.; Jang, J.-H. Nanoporous hematite structures to overcome short diffusion lengths in water splitting. *J. Mater. Chem. A* **2014**, *2*, 19999−20003.
(59) Zhou, G.; Shan, Y.; Wang, L.; Hu, Y.; Guo, J.; Hu, F.; Shen, J.; Gu, Y.; Cui, J.; Liu, L.; Wu, X. Photoinduced semiconductor-metal transition in ultrathin troilite FeS nanosheets to trigger efficient hydrogen evolution. *Nat. Commun.* **2019**, *10*, 1597.
(60) Mishra, D.; Farrell, J. Understanding nitrate reactions with zero-valent iron using tafel analysis and electrochemical impedance spectroscopy. *Environ. Sci. Technol.* **2005**, *39*, 645−650.

https://doi.org/10.1021/acs.est.2c02406
Environ. Sci. Technol. 2022, 56, 13954−13963